DISCRETE SCINTILLATOR COUPLED MERCURIC IODIDE PHOTODETECTOR ARRAYS FOR BREAST IMAGING

Martin P. Tornai, *Student Member, IEEE*, Bradley E. Patt,* *Member, IEEE*, Jan S. Iwanczyk,* *Member, IEEE*, Craig S. Levin, *Member, IEEE*, and Edward J. Hoffman, *Senior Member, IEEE*

Division of Nuclear Medicine & Biophysics, Department of Molecular & Medical Pharmacology, UCLA School of Medicine, Los Angeles, CA 90095
**Advanced Detectors Inc., 1220-A Avenida Acaso, Camarillo, CA 93012*

ABSTRACT

Multi-element (4x4) imaging arrays with high resolution collimators, size matched to discrete CsI(Tl) scintillator arrays and mercuric iodide photodetector arrays (HgI_2 PDA) were developed as prototypes for larger 16x16 element arrays for breast imaging. The compact nature of the arrays allows detector positioning in close proximity to the breast to eliminate activity not in the line-of-sight of the collimator, thus reducing image background. Short collimators, size matched to $\leq$1.5x1.5 mm^2 scintillators show a factor of 2 and 3.4 improvement in spatial resolution and efficiency, respectively, compared to high resolution collimated gamma cameras for the anticipated compressed breast geometries. Monte Carlo simulations, confirmed by measurements, demonstrated that scintillator length played a greater role in efficiency and photofraction for 140 keV gammas than cross sectional area, which affects intrinsic spatial resolution. Simulations also demonstrated that an increase in the ratio of scintillator area to length corresponds to an improvement in light collection. Electronic noise was below 40 e^- RMS indicating that detector resolution was not noise limited. The high quantum efficiency and spectral match of prototype unity gain HgI_2 PDAs coupled to 1x1x2.5 mm^3 and 2x2x4 mm^3 CsI(Tl) scintillators demonstrated energy resolutions of 9.4% and 8.8% FWHM at 140 keV, respectively, without the spectral tailing observed in standard high-Z, compound semiconductor detectors. Line spread function measurements matched the scintillator size and pitch, and small, complex phantoms were easily imaged.

I. INTRODUCTION

Standard X-ray mammography is accepted as the best means of screening for non-palpable breast cancer. However, signatures of breast cancer, such as microcalcifications or masses that are seen for most malignant lesions may also be associated with benign processes. Thus, while the sensitivity of mammography is on the order of 85%, its specificity is limited to only 20-30%, and only about 30% of the biopsies based on mammographic findings are positive [1,2].

Recent imaging studies with radiopharmaceuticals (e.g. ^{99m}Tc-Sestamibi; 140 keV gamma rays) and standard gamma cameras have shown uptake in tumors, apparently in proportion to the malignancy of the tumor [3-8]. Specifically, the rapid uptake mechanism of Sestamibi fixes the compound in place and minimizes redistribution. Recent reports on detection of breast tumors using Sestamibi, all give sensitivities and specificities in the neighborhood of 90% [3-10]. Equally encouraging results have also been reported for ^{99m}Tc-Methylene Diphosphonate with a sensitivity of 92% and a specificity of 95% [11]. Whereas these previous studies showed uptake of ~4:1 tumor to background in breasts, a recent standard scintillation camera scintimammography study along with excised breast tissue demonstrated uptake of 6.1 to 1 tumor to fatty breast tissue [8]. The excised samples included smaller masses (<1 cm^3) missed with scintimammography. These studies not only corroborate measurements of the excellent uptake achievable with Sestamibi, but they also demonstrate the need for a compact, high resolution and sensitivity nuclear emission imaging device which might detect these otherwise missed, smaller lesions.

In this work, we investigate a novel imaging detector array prototype composed of high efficiency CsI(Tl) scintillators coupled to high quantum efficiency and low noise solid state mercuric iodide (HgI_2) photodetector arrays (PDAs). The major issues considered include the possibility for improved energy and spatial resolution compared with standard gamma cameras, as well as improved detector efficiency and photofraction compared with intrinsic semiconductor detectors. In general, scintillators facilitate higher gamma stopping efficiencies compared to high-Z compound semiconductor detectors of equivalent stopping thicknesses without the low energy spectral tailing observed due to poor charge collection. Another advantage of this scintillator-photodetector combination is the higher achievable photofraction which is degraded by the row/column coincidence criteria employed with intrinsic HgI_2 semiconductor detector arrays [12].

In addition, the camera's size should be small enough that it could be used in conjunction with mammography breast compression fixtures allowing it to optimally image the breast. The angle would be chosen to image the breast and the axillary lymph nodes while minimizing the amount of heart or liver activity in the field-of-view (FOV), resulting in further improvements in resolution and signal-to-noise over standard gamma cameras. In a larger version, this camera combined with the appropriate radiotracer could be used as the primary screening test for those patients with dense breasts or other conditions that would compromise the usefulness of standard X-ray mammography. The parameters investigated include the limiting effects of the collimator, the feasibility of using small, discrete scintillation detectors coupled to solid state photodetectors, and the combined effects of these components on gamma detection efficiency and sensitivity, energy and spatial resolution, as well as imaging ability.

II. OPTIMIZATION OF DETECTOR DESIGN

There are two primary innovations in the approach of this work. First, the collimator hole openings exactly match the detector sizes, and the collimator septal thickness corresponds with the inter-crystal spacing in order to maximize the signal for any given detector element in the array. Second, the use of high efficiency and high intrinsic spatial resolution detectors

0018-9499/97$10.00

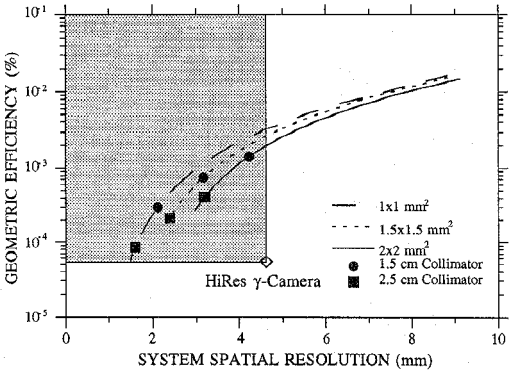

FIGURE 1. Geometric efficiency vs system spatial resolution calculated for various square hole collimator lengths with a source at 1 cm distance from collimator face; shaded region represents region of improved SNR.

in close proximity to the partially compressed breast affords a transition from collimator limited camera resolution, which is characteristic of Anger camera systems, to detector limited camera resolution. Standard gamma cameras, whose primary intent is to image objects at depth, are primarily limited by the collimator characteristics. On the other hand, in an application specific device for high resolution imaging, relatively shallow object imaging will be limited by the intrinsic detector properties.

A. Collimator Effects on Signal-to-Noise

In single photon imaging, the collimator limits the overall system spatial resolution and sensitivity [13]. One important reason for choosing a matched collimator opening to detector size is that the point source geometric efficiency for a parallel hole collimator with ≤2 mm x 2 mm square detectors is better than that for a standard commercially available high resolution (HiRes) gamma camera (hexagonal, 1.5 mm hole diameter, 4 cm length) currently used in scintimammography. For example, a design with a 2.5 cm long collimator size matched to a 1.5 mm square crystal has 3.4 times better efficiency performance than a standard HiRes collimator, along with superior spatial resolution (Fig. 1). Thus, an efficiency gain is due to the larger exposed area of each detector crystal with the collimator openings size matched to the detectors. The collimator septa overlap the intercrystal reflector (dead) spaces.

These collimator parameters affect the time required to collect adequate events from breast lesions with various radiotracer uptake values (10 min, 2.1 tumor / background [3]), with higher efficiencies leading to shorter imaging times. Improved geometric efficiency will lead to (1) improved statistics for the same imaging time, or (2) reduced imaging time, or (3) reduced patient dose.

Spatial resolution is also important in this application due to the necessity of discerning small tumors (<1 cm diameter). However, improving spatial resolution by increasing collimator length penalizes efficiency (Fig. 1). For Anger camera systems used to image relatively distant objects, system resolution degradations are limited by the collimator optics [13]. For the proposed high intrinsic resolution system to image objects in close proximity, the system resolution will be limited by the intrinsic spatial resolution rather than the collimator. Thus, shorter more efficient collimators can be utilized without a resolution degradation. The expected performance for the proposed breast imaging camera geometry lies in a region that is always superior to HiRes nuclear medicine gamma cameras (Fig. 1), which are currently used as the standard for scintimammography imaging [3-7]. The factors that yield the improved signal-to-noise ratio (SNR) for this system include (1) improved spatial resolution compared to the standard HiRes system, (2) improved geometric efficiency, and (3) reduced background due to both the vantage point of the camera, which will eliminate the body (e.g. heart, liver) from background, and the use of partial compression, and also (4) the improved scatter rejection techniques due to the excellent energy resolution (see *III.A.*).

The compact nature of our imaging device, due to the anticipated short collimator, small scintillators (see *II.B.*), flat HgI_2 PDA (see *II.C.*), and thin ASIC readout electronics in contact with the detector will facilitate close detector to source proximity, such as from a medio-lateral or latero-medial vantage point of the breast. With partial breast compression, maximum tissue thicknesses of 5 cm can be anticipated, and our imaging device can be positioned to get opposing views of a breast to take advantage of the higher achievable resolution at short distances, and ensure that the detector would not be more than 2.5 cm from any lesion. Standard gamma cameras cannot easily get either superior-inferior or lateral opposing views due to physical limitations or interference from the head, stomach or contra-lateral chest wall, which may also contribute radioactive shine into the detector. The physical distance poses a serious problem for opposing views of the same breast with a standard gamma camera which is overcome by our design.

A conservative estimate of the background reduction is a factor of 2, due to partial breast compression (bringing the breast thickness to <5 cm), latero-medial positioning of the camera, and the improved scatter rejection. With uptake values for ^{99m}Tc-Sestamibi measured with standard cameras at ≥2 tumor to background, the background reduced image contrast will nominally improve by 33%. These factors alone will improve the image quality significantly [14].

Most importantly the improved spatial resolution will enable visualization of smaller tumors (~2x2 mm^2) than previously achievable with the HiRes gamma camera. For example, for large tumors (>2x2 cm^2), both cameras will resolve the tumors and recover approximately 100% of the activity distribution in the image. However, for a tumor at 2.5 cm depth in the breast, the HiRes gamma camera has a resolution of 4.9 mm; thus for a relatively small 0.4x0.4 cm^2 tumor [3] the activity recovery in the FOV is only ~40%, which severely limits it's detectability. Due to the improved spatial resolution of our proposed device (3.4 mm for this depth) along with closer proximity, the activity recovery will be improved by at least 56% (improvement is in tumor visualization, i.e. image contrast).

B. Simulations to Optimize Small Detectors

Thick scintillators offer higher gamma stopping efficiencies without the low energy spectral tailing observed in high-Z compound semiconductor detectors of equivalent stopping thicknesses. Thus, several factors were considered when choosing parallel-piped CsI(Tl) scintillators for use with the HgI_2 PDA. CsI(Tl) has a better mass absorption coefficient at 140 keV than NaI(Tl) (4.47 cm^{-1} and 2.98 cm^{-1}, respectively).

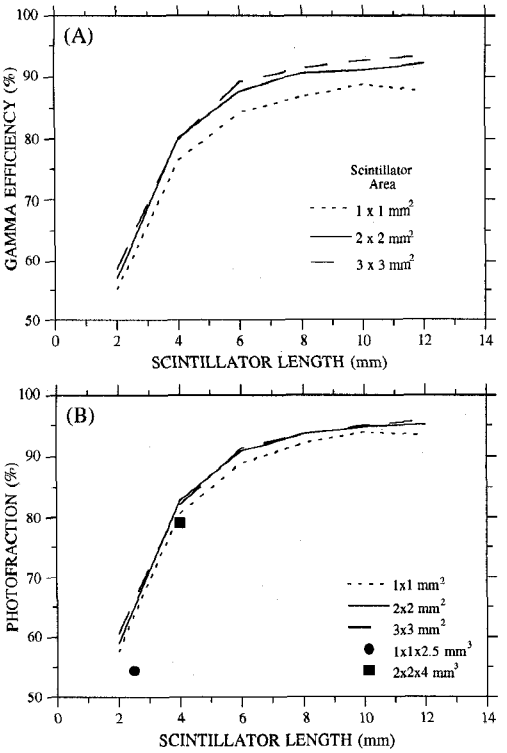

FIGURE 2. (A) Simulation results for total gamma efficiency for ^{57}Co gamma rays in small CsI(Tl) crystals. (B) Simulated and measured photofraction results with same irradiation conditions.

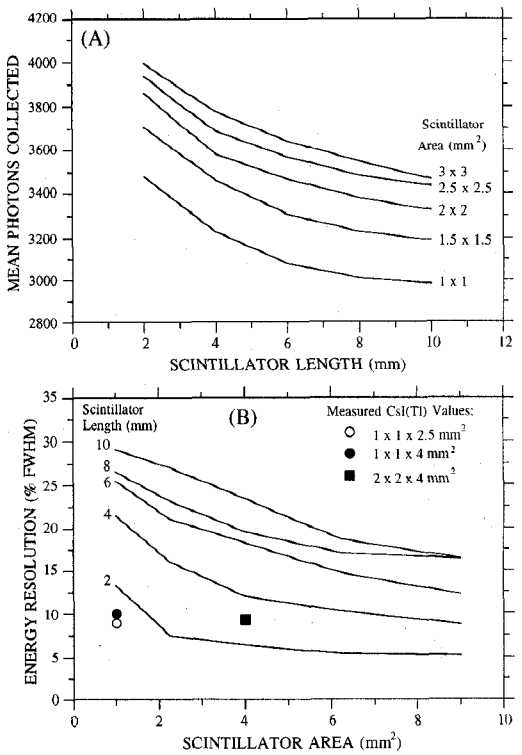

FIGURE 3. Simulation results and measurements of ^{57}Co irradiated small CsI(Tl) crystals coupled to HgI2 PDAs demonstrating effects of crystal geometry on light collection (A) and effects on resolution (B). Simulations assumed 98% reflectivity and 70% photodetector QE.

CsI(Tl) has a peak visible emission wavelength of 530 nm which corresponds well to the absorption maximum of 560 nm in the HgI_2 photodetector, and also produces ~35% more photons than NaI(Tl) for equivalent energy deposition. Short parallel-piped crystals offer equivalent light collection compared with cylindrical crystals of similar dimensions, degrading with longer (>2 cm) lengths [15], and are also more easily manufactured in large quantities.

The QE of the HgI_2 PD is near 100% from 350 to 560 nm [16], and is slightly degraded by the optical contact (see *II.C.*). Mercuric iodide detectors coupled to CsI(Tl) scintillators have now demonstrated perhaps the best energy resolution at room temperature ever attained by any scintillator / photodetector pair (4.58% FWHM at 662 keV for a 0.5 in. diameter photodetector [17]). Thus, the emission-absorption wavelength match and light output properties of the scintillator are well suited for use with HgI_2 PDAs, and the superior stopping efficiencies facilitate the use of smaller crystals. Monte Carlo simulations and measurements were utilized to help determine the effects of scintillator crystal size and surface treatment for detectors in the imaging array.

With a gamma-ray multiple scattering Monte Carlo code [18], several small CsI crystals from 1x1x2 mm^3 up to 3x3x 12 mm^3 were modeled. The resultant energy deposition and position information was further utilized in an optical tracking Monte Carlo code [19] which modeled surface treatments on the scintillation crystals coupled to the HgI_2 photodetectors.

The simulation results from flood field gamma interactions with ^{57}Co (122 keV (88%) and 136 keV (12%)) in various sized individual parallel-piped CsI(Tl) scintillators indicate that for ≥5 mm crystal lengths, the efficiency for various discrete scintillators was >80% (Fig. 2A). Note that for increasing crystal length, the rate of improving efficiency is dramatic up to about 6 mm in length beyond which the rate of improvement roles off and then only slowly improves with thickness. The trends for photofraction are similar to the total gamma efficiency trends (Fig. 2B), and these results indicate that the dominant interactions in these small crystals is photoelectric. Measured photofraction values (defined as the integral counts from 105-160 keV about the photopeak divided by the total detected events) for two crystal sizes (see *III.A.*) agree well with the simulation results.

The optimal surface treatment as determined by the combined simulations of a 2x2x6 mm^3 crystal were consequently used in all further simulations. With the distal surface from the photodetector ground and sides of the scintillator specularly polished, the best light collection was achieved (~75% collection), corresponding with results of other work [15,20].

The optical simulation results indicate that light collection from a parallel-piped CsI(Tl) scintillator increases with decreasing length, and more slowly increases with increasing surface area (Fig. 3A). With an absolute charge calibration of the HgI_2 photodetector array measured with ^{55}Fe (5.9 keV X-ray) direct detection, the measured light collection values are within 5-15% of the predicted values. These results also correspond with other data for similar simulations and measurements [15,20]. The measured FWHM energy resolutions with ^{57}Co irradiation were better than some of the Gaussian fit photopeak simulation results (Figs. 3B and 5). While the simulation assumptions may not have accurately predicted the measured results (see *III.A.*), the trends in improving energy resolution are consistent with the light collection characteristics. We are nonetheless encouraged that the preliminary measurements are indeed better than the predicted values in our

effort to optimize the imaging system.

C. Scintillator and Photodetector Arrays

Segmented CsI(Tl) scintillators with sixteen segments each either 1x1 mm^2 in area with 2.5 or 4 mm lengths, or 2x2x4 mm^3 were procured from Hilger Analytical Ltd. The segments are arranged in a two dimensional 4x4 pattern and separated by TiO_2 doped epoxy of 0.2 mm or 0.5 mm thickness.

The fabricated HgI_2 PDAs have 16-pixels each with either 1x1 mm^2 pixels or 2x2 mm^2 pixels with gaps corresponding to the crystal separation. The pixels are defined through the geometry of the metal contact deposition on the back side of the 560 μm HgI_2 wafer.

The front side contact utilized electrically conductive ultra-thin metal contacts which are optically transparent, and non-reactive with HgI_2. By carefully applying the evaporation in a vacuum bell jar, uniform metalization layers with transmissions up to 70% from 400 to >1000 nm were achieved with sheet resistance of <500 Ω/square for thin layers. These transmission properties are good for CsI(Tl) light but do degrade the overall detector QE to about 70%.

D. Photodetector Noise Considerations

One of the main considerations for unity gain solid state photodetectors is the noise level. By using a particular construction, the HgI_2 photodetector technology can circumvent the well known problem associated with hole trapping in high-Z compound semiconductors. Optical photons penetrate only a very shallow region beneath the entrance electrode, and with negative entrance electrode bias, only the electrons transit the device. The charge collection becomes essentially single carrier (electron) dominated. With electron transit times ($\tau_{transit}$ ~ 5 x 10^{-7} sec) almost 10 to 100 times faster than electron trapping times ($\tau_{trapping}$= 10^{-5}-10^{-6} sec) in HgI_2, almost complete charge collection is expected.

For all spectral and imaging measurements, each pixel from the PDA (16 total) is coupled to a customized, low noise, charge sensitive, resistor feedback preamplifier (Advanced Detectors). Photopeak broadening due to electronic noise was determined by comparing the ^{55}Fe direct X-ray interactions in the HgI_2 detector with the photo response from CsI(Tl). This approach relates easily measurable material constants by a scale factor which is inversely proportional to the efficiency for light generation and collection. The "direct" noise line-width is a combination of the noise power terms which includes series, parallel, and excess (1/*f* and generation-recombination) noise components and was previously calculated [21,22]. The total noise contributions are in excellent agreement with measured pulser data on a fully biased detector (Fig. 4A). A minimum linewidth was achieved with ~6 μsec shaping time. The average pulser width with full bias on the detector for the 16 channels was about 368 eV and 400 eV FWHM for the 1x1 mm^2 and 2x2 mm^2 pixels, respectively, corresponding to 37 e^- and 41 e^- RMS at 6 μsec shaping time.

The ^{57}Co photopeak resolution and electronic noise (pulser method) were also measured for the 2x2x4 mm^3 scintillator crystals as a function of shaping time using a representative pixel. While theory predicted an optimum shaping time of ~6 μsec (Fig. 4A), the scintillator coupled PDA measurement results improved further with increased shaping time (measured

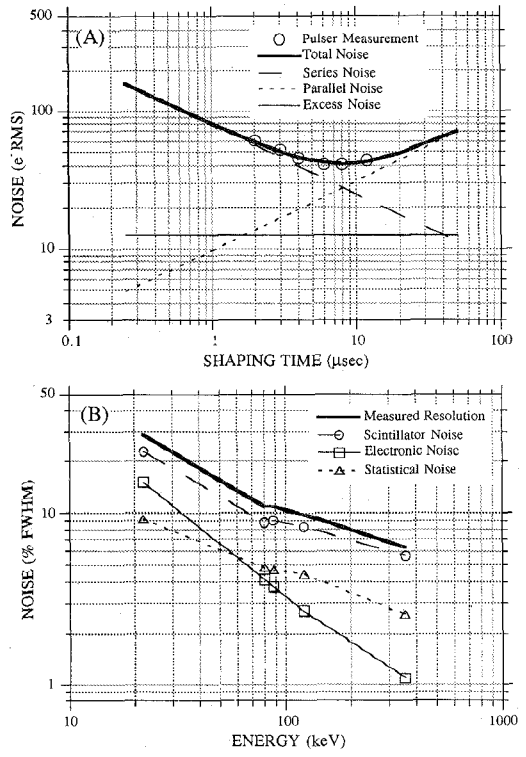

FIGURE 4. (A) Theoretical noise calculations for a 2x2 mm^2 element as a function of shaping time compared with measured pulser data. (B) Measured resolution values and component contributions to the overall spectral linewidth, measured with 12 μsec, triangular shaping.

up to 12 μsec, triangular shaping). This may be due to contributions of longer CsI(Tl) scintillator decay components rather than incomplete electron charge collection since much longer shaping times were used compared to the $\tau_{transit}$. This is similar to other results of CsI(Tl) scintillators coupled to PIN diode detectors [15].

The overall spectral linewidth corresponds to (Fig. 4B): (1) the electronic noise; (2) the intrinsic noise in the scintillator, which is a function of the scintillator material and photon energy; (3) the statistical spreading (light transfer and collection efficiency, and detector QE). The degradative effects of these factors are assumed to add in quadrature to the total resolution. The factors are measured parameters, except for the scintillator noise which is calculated according to [23]. The dominant factor in the spectral linewidth is the scintillator. For less efficient light collection, as from long crystals (cf. Fig. 3), the dominant factor varies as a function of energy, with electronic noise dominating at low energies, and intrinsic scintillator noise dominating at high energies. The crossover point at which these contributions are equal has been found empirically to be about 60-100 keV (Fig. 4B). Thus for ^{99m}Tc tracer studies (140 keV), lowering the electronic noise is crucial and was satisfactorily achieved.

III. Imaging Detector Characteristics

A. Detector Spectral Responses

The pixel responses were measured by individually connecting each of the sixteen preamplifiers to a Tennelec TC244 tri-

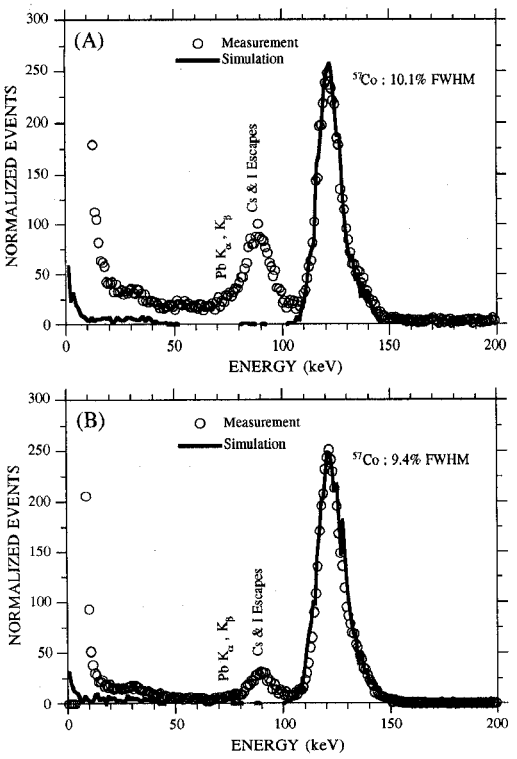

FIGURE 5. Measured spectral responses compared with simulations with 4.8 keV noise for (A) 1x1x2.5 mm^3 crystals and (B) 2x2x4 mm^3 crystals coupled to 1x1 mm^2 and 2x2 mm^2 photodetectors.

angular shaping (12 μsec) amplifier feeding a standard MCA. The response of each of the sixteen individual pixels with the 2x2 mm^2 PDA with the 2x2x4 mm^3 CsI(Tl) crystals was measured with ^{241}Am (59 keV) and ^{57}Co (122 keV) collimated sources. The average energy resolution for all 16 pixels was 13.55% ± 0.86% FWHM at 59 keV, and 10.49% ± 0.64% FWHM at 122 keV. At 140 keV, these values scale to <10% FWHM which is comparable to the best values achieved with standard gamma cameras.

The spectral characteristics for pixels from both the 1x1x2.5 mm^3 and 2x2x4 mm^3 crystals agree well with high statistics Monte Carlo simulation results (Fig. 5). Note, however, that the simulations did not accurately account for the measured escape peaks or Compton continuum. The measured energy resolutions of the 122 keV photopeaks are 10.1% and 9.4% FWHM for the 1 mm and 2 mm pixels, respectively. The energy resolutions of the simulations range from 8.2% - 10.6% and 8.7% - 12.4% FWHM for the 1x1x2.5 mm^3 and 2x2x4 mm^3 scintillators, respectively, depending on the 2.5 - 4.8 keV noise contribution. The noise values were derived from the direct/photo calibration (see *II.D.*).

The measured photofractions (integral counts from 105 to 160 keV divided by the integral counts from 20 to 160 keV) were 54.4% and 79.1% for the 1 mm and 2 mm crystals, respectively (Figs. 2 and 5). The fraction of counts integrated over the region including the Pb K_α, K_β, and Cs and I escape peaks are 26% and 12% for the 1 mm and 2 mm crystals, respectively, which is a function of the increased efficiency of the larger volume scintillator.

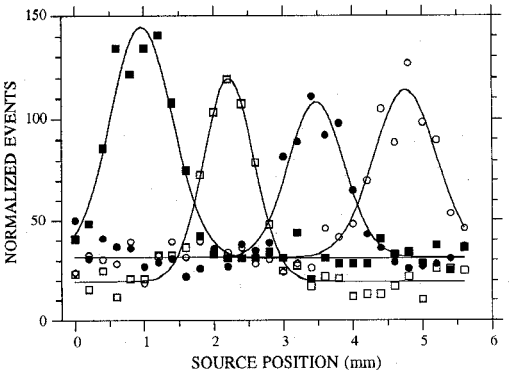

FIGURE 6. LSF response function for a single inner column of the 1x1x2.5 mm^3 CsI(Tl) crystals coupled to the HgI_2 PDA.

B. Detector Spatial Responses

The spatial response and imaging measurements were made with the low noise preamplifier outputs coupled to CAMAC programmable shaping amplifiers with variable shaping times, variable gain, and SCAs for each channel which provided a logic signal for events above a minimum threshold (Advanced Detectors). A 4.8 μsec shaping time was used with individually balanced pixel gains, and the amplifier outputs were digitized with a peak sensing CAMAC ADC (16 channel Phillips 7164). The logic signals from the SCA outputs were linearly ORed in a double gating (long blocking gate, short ADC trigger gate with leading edge discrimination) CAMAC module with NIM level output (Advanced Detectors) which triggered the ADCs. The data acquisition and control was with LabVIEW™ (National Instruments) on an 150 MHz Pentium™ based PC (Gateway). All imaging data were normalized by measured flood field values to account for differences in crystal efficiencies and gains.

The intrinsic line spread function (LSF) response was measured for the 1x1x2.5 mm^3 CsI(Tl) elements coupled to the 1x1 mm^2 pixels on the PDA. A 0.3 mm Pb collimated slit source of ^{57}Co was stepped in 0.2 mm increments along the vertical direction of the 4x4 square array. The LSF response was found to correspond with the crystal dimensions (Fig. 6) with a 0.98 ± 0.10 mm mean FWHM resolution for the 1 mm crystals, and a mean centroid spacing of 1.26 ± 0.01 mm which corresponds to the detector pitch of 1.25 mm. The measured values were derived from Gaussian fits to the data.

C. Preliminary Imaging Results

Some images were acquired with ^{57}Co irradiation through a Pb transmission phantom with a complex hole pattern (Fig. 7). Since the phantom was larger than the FOV of the 4x4 element 1x1x2.5 mm^3 CsI(Tl) crystal array, multiple samples were collected and digitally spliced together. To eliminate pixellation artifacts resulting from imaging the small phantom (Fig. 7B), half-pitch offset measurements were collected and interleaved with the single step data (Fig. 7C). This interleaving measurement demonstrates the integrity and response linearity of the small imaging array, while improving the sampling of the source distribution. In addition, the subsampled data was linearly interpolated to smooth the noise. These

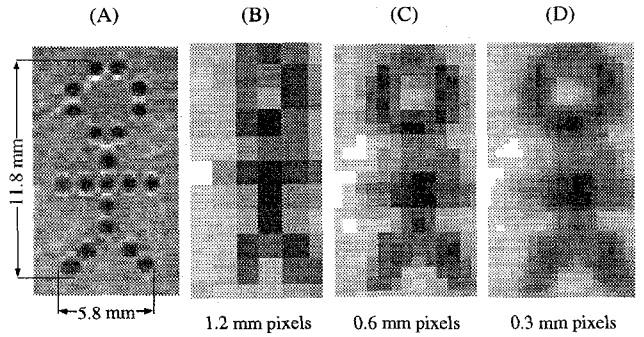

FIGURE 7. (A) Pb transmission phantom with 1.0 mm ϕ holes, (B) single stepped acquisition of (A), (C) subsampled image of (A), and (D) linear interpolation of (C). Images were acquired with the 1x1x2.5 mm^3 CsI(Tl) crystals on the 1x1 mm^2 PDA.

results indicate that the imaging device has a high degree of linearity and can distinguish complex source distributions with high resolution. Tumor sources in breasts and especially the axilla are expected to have spherical distributions potentially with spiculations or extensions into healthy tissue.

IV. Conclusions

Significant advancement has been made in the development of two dimensional HgI_2 PDA technology by incorporating previously developed and novel principles for the optimization of small photodetector array structures. Mercuric iodide PDA prototypes with 16 pixels each 1x1 mm^2 with 0.2 mm gaps, and 2x2 mm^2 with 0.5 mm gaps defined through the geometry of the metalized contact deposition on the HgI_2 wafer were fabricated. The 16 element PDAs were evaluated with segmented CsI(Tl) scintillators of various volumes and pitch corresponding to the electrode patterning on the PDAs. In addition, extensive computer simulations of energy deposition and scintillation light transport both confirmed many of our measurements, and guided us towards more optimal configurations which may surpass the already high performance of these preliminary studies.

The importance of collimators in single photon imaging is that the collimator is the limiting factor for the overall system resolution and sensitivity. Because of this limitation, we have investigated the optimization of the collimator parameters and compared the expected performance with the standard HiRes gamma camera for the specific application of high resolution and sensitivity scintimammography. Moreover, it was demonstrated that the high intrinsic spatial resolution detectors coupled to relatively short, size matched collimators could achieve better signal-to-noise characteristics than their standard Anger camera counterparts. This was achieved with the high intrinsic detector resolution and obtainable close proximity to the breast lesions, which is otherwise not possible with standard gamma camera systems.

The device itself included sufficient scintillator thickness for at least 1/e photoelectric attenuation in the scintillators. The segmented scintillators were nearly optimized for light collection while spectrally matched to the photodetector. Theoretical calculations of the expected spectral resolution and spatial resolution were made and compared favorably with the measured results. The noise performance of the 1 mm^2 and 4 mm^2 photodetectors were characterized to be ~40 e^- rms. The spatial resolution corresponded to the scintillator size. Pixel energy resolutions of the measured 122 keV photopeaks were 10.1% and 9.4% FWHM for the 1x1x2.5 mm^3 and 2x2x4 mm^3 crystals coupled to the appropriately sized PDA, respectively. The simulated energy resolutions ranged from 8.2% - 10.65% and 8.7% - 12.4% for the 1x1x2.5 mm^3 and 2x2x4 mm^3 scintillators, respectively, depending on the predicted noise contribution, and corroborated the measurements.

Moreover, the first images of a complex phantom were obtained with an assembled 4x4 element device. On the basis of the simulated and measured performance of the scintillator / HgI_2 PDA combination, we expect that a larger FOV camera will: (1) detect lesions ~5 times smaller than previously achievable (2 - 3 mm range); (2) shorten the imaging procedure with the breast under partial compression to under 5 minutes using currently published dose; and (3) improve the statistical quality of the obtained images.

Acknowledgments

The authors thank Fanny Riquelme, Jim Menjivar, Ryszard Szczebiot, Richard Koziol, George Maculewicz and David Marsh for their expert assistance on various parts of this work. This work was funded in part by NCI grants 1R43-CA68845-01, 1R01-CA61037-01, 1R43-CA69988-01, 2R44-CA61403-02, DOE contract DE-FC03-87-ER60615, and University of California IRB-0225.

References

[1] CJ Baines, *et al.* 1986. Sensitivity and Specificity of First Screen Mammography in the Canadian National Breast Screening Study: A Preliminary Report from Five Centres. *Radiology*. **160**:295-298.

[2] L Tabar, PB Dean. 1982. Mammographic Parenchymal Patterns: Risk Indicator for Breast Cancer? *J. Am. Med. Assoc.* **247**:185-189.

[3] I Khalkhali, *et al.* 1995. Scintimammography: The Complementary Role of Tc-99m Sestamibi Prone Breast Imaging for the Diagnosis of Breast Carcinoma. *Radiology*. **196**:421-426.

[4] C Aktolun, H Bayhan, M Kir. 1992. Clinical Experience with Tc-99m MIBI Imaging in Patients with Malignant Tumors: Preliminary Results and Comparison with Tl-201. *Clin. Nucl. Med.* **17**:171-176.

[5] F Scopinaro, *et al.* 1994. Tc-99m Sestamibi: An Indicator of Breast Cancer Invasiveness. *Eur. J. Nucl. Med.* **21**:984-987.

[6] C-H Kao, S-J Wang, S-H Yeh. 1994. Tc-99m MIBI Uptake in Breast Carcinoma and Axillary Lymph Node Metastases. *Clin. Nucl. Med.* **19**:898-900.

[7] I Khalkhali, I Mena, L Diggles. 1994. Review of Imaging Techniques for the Diagnosis of Breast Cancer: A New Role of Prone Scintimammography Using Tc-99m Sestamibi. *Eur. J. Nucl. Med.* **21**:357-362.

[8] J Maublant, *et al.* 1996. Tc-99m-Sestamibi Uptake in Breast Tumor and Associated Lymph Nodes. *J. Nucl. Med.* **37**:922-925.

[9] I Khalkhali, *et al.* 1995. Tc-99m-Sestamibi Scintimammography of Breast Lesions: Clinical and Pathological Follow-Up. *J. Nucl. Med.* **36**:1784-1789.

[10] R Taillefer, A Robdoux, R Lambert, S Turpin, J Laperriere. 1995. Tc-99m-Sestamibi Prone Scintimammography to Detect Primary Breast Cancer and Axillary Node Involvement. *J. Nucl. Med.* **36**:1758-1765.

[11] S Piccolo, *et al.* 1995. Tc-99m-Methylene Diphosphonate Scintimammography to Image Primary Breast Cancer. *J. Nucl. Med.* **36**:718-724.

[12] BE Patt, JS Iwanczyk, MP Tornai, CS Levin, EJ Hoffman. 1995. Development of a Mercuric Iodide Detector Array for Medical Imaging Applications. *Nucl. Instr. Meth.* **A366**:173-182.

[13] BMW Tsui. Collimator Design, Properties and Characteristics. In *The Scintillation Camera*. Ed. GH Simmons. The Society of Nuclear Medicine, Inc. New York. 1988. Ch. 2.

[14] BMW Tsui, CE Metz, RN Beck. 1983. Optimum Detector Spatial Resolution for Discriminating Between Tumor Uptake Distributions in Scintigraphy. *Phys. Med. Biol.* **28**:775-788.

[15] AJ Bird, T Carter, AJ Dean, D Ramsden, BM Swinyard. 1993. The Optimisation of Small CsI(Tl) Gamma-Ray Detectors. *IEEE Trans. Nucl. Sci.* **NS-40**:395-399.

[16] JM Markakis, AY Cheng. 1989. Comparison of Transparent Conducting Electrodes on Mercuric Iodide Photocells. *Nucl. Instr. Meth.* **A283**:236-239.

[17] YJ Wang, BE Patt, JS Iwanczyk, SR Cherry, Y Shao. 1995. High Efficiency CsI(Tl)/HgI_2 Gamma Ray Spectrometers. *IEEE Trans. Nucl. Sci.* **NS-42**:601-605.

[18] Y Shao, SR Cherry, S Siegel, RW Silverman. 1996. A Study of Intercrystal Scatter in Small Scintillator Arrays Designed for High Resolution PET Imaging. *IEEE Trans. Nucl. Sci.* **NS-43**:1938-1944.

[19] GF Knoll, TF Knoll, TM Henderson. 1988. Light Collection in Scintillation Detector Composites for Neutron Detection. *IEEE Trans. Nucl. Sci.* **NS-35**:872-875.

[20] SR Cherry, *et al.* 1995. Collection of Scintillation Light from Small BGO Crystals. *IEEE Trans Nucl. Sci.* **NS-42**:1058-1063.

[21] JS Iwanczyk, BE Patt. In *Semiconductors for Room Temperature Nuclear Detector Applications.* Vol 43. Eds. TE Schlesinger, RB James. Academic Press. 1995. pp. 615-624.

[22] BE Patt, *et al.* 1996. Mercuric Iodide Photodetector Arrays for Gamma-Ray Imaging. *Nucl. Instr. Meth.* **A380**:295-300.

[23] JM Markakis. 1988. Mercuric Iodide Photodetector-Cesium Iodide Scintillator Gamma Ray Spectrometers. *IEEE Trans. Nucl. Sci.* **NS-35**(1):356-359.